

Article

Secondary High-Temperature Treatment of Porous Carbons for High-Performance Supercapacitors

Weihao Chi, Guanwen Wang, Zhipeng Qiu , Qiqi Li, Zheng Xu, Zhiyuan Li, Bin Qi, Ke Cao, Chunlei Chi , Tong Wei and Zhuangjun Fan  *

School of Materials Science and Engineering, China University of Petroleum (East China), Qingdao 266580, China

* Correspondence: chichunleiccl4@163.com (C.C.); fanzhj666@163.com (Z.F.)

Abstract: Supercapacitors are extensively used in urban rail transit, electric vehicles, renewable energy storage, electronic products, and the military industry due to its long cycle life and high power density. Porous carbon materials are regarded as promising anode materials for supercapacitors due to their high specific surface areas and well-developed pore structures. However, the over-developed pore structure often results in poor conductivity and reduced cycle stability due to the destruction of a carbon skeleton. Herein, we introduce an advanced strategy for preparing porous carbon with high specific surface areas ($3333\text{ m}^2\text{ g}^{-1}$), high electrical conductivity (68.6 S m^{-1}), and fast ion transport channels through secondary high-temperature carbonization treatment. As a result, the fabricated porous carbon anode delivers a high specific capacitance (199.2 F g^{-1} at 1 A g^{-1}) and outstanding rate performance (136.3 F g^{-1} at 20 A g^{-1}) in organic electrolyte. Furthermore, the assembled symmetrical supercapacitor achieves an energy density of 43.2 Wh kg^{-1} at 625.0 W kg^{-1} , highlighting the potential of a secondary high-temperature carbonization strategy in practical applications.

Keywords: supercapacitors; porous carbon; secondary high-temperature carbonization



Citation: Chi, W.; Wang, G.; Qiu, Z.; Li, Q.; Xu, Z.; Li, Z.; Qi, B.; Cao, K.; Chi, C.; Wei, T.; et al. Secondary High-Temperature Treatment of Porous Carbons for High-Performance Supercapacitors. *Batteries* **2024**, *10*, 5. <https://doi.org/10.3390/batteries10010005>

Academic Editor: Leon L. Shaw

Received: 4 December 2023

Revised: 19 December 2023

Accepted: 22 December 2023

Published: 25 December 2023



Copyright: © 2023 by the authors. Licensee MDPI, Basel, Switzerland. This article is an open access article distributed under the terms and conditions of the Creative Commons Attribution (CC BY) license (<https://creativecommons.org/licenses/by/4.0/>).

1. Introduction

Environmental challenges and the restricted availability of fossil fuels have promoted the great development and application of environmentally friendly renewable energy, such as solar energy, geothermal energy, wind energy, tidal energy, and hydrogen energy [1–5]. However, sustainable energy is inherently intermittent and unevenly distributed in terms of time and space. Thus, energy storage devices (ESDs) with a high energy density, long cycle life, and power density are eagerly demanded. Among various ESDs, supercapacitors (SCs) have become increasingly important as a short-term energy storage buffer due to their high power densities, long lifespans, great safety, and adaptability to temperature [6–8]. Nevertheless, the limited energy density hinders the further application of SCs.

Based on the previous research, enlarging the voltage window and increasing capacitance are both effective to improve the energy density of SCs [9,10]. Chang et al. [11] reported a frame-filled C/C composite with coal tar pitch and natural flake graphite as raw materials, showing both a high specific surface area and electrical conductivity. When tested in the TEABF₄ in the PC electrolyte (3 V) and medium pure EMIMBF₄ electrolyte (3.5 V), the C/C composite exhibited both high gravimetric and volumetric capacitances. Moreover, it displayed a high energy density as high as 66.3 Wh kg^{-1} . Similarly, Leng et al. [12] synthesized a three-dimensional carbon framework (3DCF) under H₂/Ar at high temperature, with a high specific surface area and good conductive network, exhibiting both ultra-fast and high charge storage. Dead leaves of Ginkgo biloba were used as the precursor to prepare activated carbon by using different activating agents [13]; the carbon activated by KOH showed the highest specific capacitance of 374 F g^{-1} at a current density of 0.5 A g^{-1} . Further, the energy density can reach 9.2 Wh kg^{-1} at a power density of 48 W kg^{-1} . Compared to SCs with the aqueous electrolyte working within 1 V, organic

electrolyte-based SCs provide a wider voltage range of 2.5–2.7 V, contributing to the higher energy density of SCs [14]. However, organic electrolytes always consist of large-sized ions, resulting in sluggish ion diffusion [15]. Therefore, the preparation of electrode materials with both plentiful energy storage active sites and rapid transport rates for large-size ions is crucial for the higher energy density of SCs. Improving specific surface areas (SSAs) of electrode materials is one effective method to enhance the ion transport rate because it can expose more active sites for the rapid physical adsorption of TEA⁺ ions [16,17]. In addition, according to the definition equation of capacitance: $C = \epsilon_r \epsilon_0 A / d$, the increase in SSAs can help increase the capacitance.

Porous carbons with high SSAs and hierarchical pore structures are the most common material used for the electrode material of commercial SCs [18]. Due to the physical adsorption and desorption, charge is stored in the Helmholtz bilayer at the electrolyte–electrode interface, resulting in the rapid ion storage capability. Moreover, porous carbon materials can generally be produced by a variety of synthesis methods, with a wide range of raw material sources and relatively low costs. Early strategies focused on exposing larger SSAs to further increase the energy storage active sites and enhance capacitance [19]. Nevertheless, the excessive increasing of SSAs and porosity will probably block the formation of continuous electron pathways, restricting the rapid charge transport and lowering the electric conductivity of active materials. Therefore, balancing the relationship among the SSAs, conductivity, and cycling stability of porous carbon has become the current research focus.

To address these issues, we propose an optimized porous carbon with the secondary high-temperature treatment strategy after the activation of phenolic resin. On the one hand, the preferential removal of oxygen-containing functional groups inside the pores at high temperatures can enlarge the transport channels and reduce the diffusion barriers of ions. On the other hand, the repeated carbonization treatment promotes the formation of more micropores and enhanced SSAs, resulting in more energy storage active sites for ion storage. In addition, the released oxygen impurities lead to the formation of a coherent conductive carbon skeleton with effectively enhanced electric and ionic conductivity. As a result, the synthesized porous carbon exhibits excellent specific capacitance (199.2 F g^{-1} at 1 A g^{-1}) and rate performance (136.3 F g^{-1} at 20 A g^{-1}). When assembled as the symmetrical SCs, it also displays a high energy density of 43.2 Wh kg^{-1} at a power density of 625.0 W kg^{-1} , demonstrating significant potential for large-scale application.

2. Materials and Methods

2.1. Materials

The materials used in this experiment included phenolic resin (chemistry), concentrated hydrochloric acid (HCl, AR), polytetrafluoroethylene (60 wt%), ethyl alcohol (AR), potassium hydroxide (AR), N₂, foamed nickel, and ketjen black. The heat-resistant phenolic resin (phenolic resin foam) is formed by the phenolic resin as the matrix and hexamethylenetetramine as the curing agent, which exhibits the internal linear or branched-chain polymer chains connected by covalent bonds, resulting in a network polymer structure. The electrolyte used in the system is 1 mol L^{-1} TEABF₄ in PC. The phenolic resin foam was ball-ground into powder before being used. Other reagents for experiments are purchased and used directly.

2.2. Preparation of High-Temperature Treated Porous Carbons (HTCs)

The high-temperature treated porous carbons (HTCs) were synthesized by a secondary high-temperature treatment strategy. Firstly, 1 g of phenol-formaldehyde resin was added to the solution of KOH (3 g) in deionized water (20 mL). The mixture was stirred for 30 min to homogenous dispersal. Subsequently, the solution was dried in oven at 100 °C, then the obtained product was ground into powder. Afterward, the powder was carbonized at 900 °C for 2 h. After chemical activation, the obtained mixture was immersed in 1 mol L^{-1} HCl solution for 12 h to remove residual K components. After filtering and drying, the sample was carbonized for the second time at 1000 or 1100 °C for 2 h. The resulting

samples were named HTC-1000 and HTC-1100, respectively. In addition, the sample without secondary high-temperature treatment is named HTC-0.

2.3. Material Characterization

Scanning electron microscopy (SEM, Hitachi Regulus 8100, Hitachi, Japan) was used to characterize the morphology and structure of the HTCs. The X-ray diffraction (XRD, Bruker Focus D8, Bruker, Germany) was used to characterize the crystal structure of the HTCs. The HORIBA Scientific LabRAM HR Evolution (Gières, France) spectrometer was used to characterize Raman spectroscopy. The magnification of the objective lens is $50\times$, the focal length of the spectrometer is 800 mm, and the spectral resolution is 1 cm^{-1} with a wavelength of 532 nm. The ESCALAB 250 Xi spectrometer (Thermo Fisher, Waltham, MA, USA) was used to characterize the X-ray photoelectron spectroscopy (XPS) of the HTCs. The ITRACER-100, (Shimadzu, Japan) was used to characterize the Fourier-transform infrared spectrum (FTIR) of the HTCs. The N_2 adsorption–desorption isotherms for HTCs were characterized by Quanta chrome IQ2 at $-196\text{ }^{\circ}\text{C}$.

2.4. Electrochemical Measurements

The slurry was mixed with active materials (HTCs), conductive carbon black, and binder (PTFE) in a mass ratio of 75:20:5. Firstly, a small amount of anhydrous ethanol and a certain mass of diluted PTFE solution was added to the conductive carbon black and ultrasonicated homogeneously. Secondly, a certain mass of active substance was added and ultrasonicated again until they were mixed homogeneously, and the obtained homogeneously mixed slurry was put into a vacuum oven for drying. Thirdly, after weighing the material of $\sim 2\text{ mg cm}^{-2}$, ethanol was added onto the material by drops for ease of rolling the material into the sheet and the sheet was pressed into a stainless-steel mesh. Finally, the pressed electrode sheets were dried in oven at $80\text{ }^{\circ}\text{C}$. The prepared supercapacitor assembly was pressed into the cell in the order of the negative case, spacer, electrode sheet, diaphragm, electrode sheet, and positive case. Before pressing, the electrolyte was injected into the supercapacitor to ensure that the electrolyte fully saturates the electrodes. In addition, symmetrical SCs were assembled using two identical electrodes in the CR2032 coin cell with cellulose diaphragm TF4035 as the separator. The organic electrolyte was 1 mol L^{-1} TEABF₄ in PC solution with a voltage window of 0–2.5 V. The CHI660E electrochemical workstation was used to conduct the electrochemical properties of cells at $25\text{ }^{\circ}\text{C}$. The rate range of galvanostatic charge-discharge (GCD) was from 1 to 20 A g^{-1} , and the current density of cyclic voltammetry (CV) was from 10 to 200 mV S^{-1} . The electrochemical impedance spectroscopy was measured at the frequency range of 0.01 to 100 kHz.

3. Results and Discussion

High-temperature treatment carbons (HTCs) were prepared by a secondary high-temperature treatment strategy after the KOH activation of phenolic resin (Figure 1). After high-temperature treatment, the order degree of amorphous carbon increased and the partial oxygen impurities were removed, resulting in excellent electrical conductivity and open ions transport channels, which is good for the rate capability of porous carbon materials [20]. Simultaneously, the pore volume and SSAs increased, which can introduce more electrochemical active sites and further increase specific capacitance for SCs [21–23]. A scanning electron microscopy (SEM) image of HTC-0 shows a block structure with a size of $20\text{--}40\text{ }\mu\text{m}$ (Figure 2a). After carbonizing at $1000\text{ }^{\circ}\text{C}$ for the second time, HTC-1000 still consists of chunks of different blocks, which is consistent with HTC-0 (Figures 2b and S1). This means that HTC-0 has excellent structural stability and there was no chalking after the high-temperature treatment. The excellent strength and toughness make the active materials bond tightly and maintain integrity during the charge and discharge process. The corresponding EDS mappings shown in Figure 2d,f demonstrate the uniform distribution of C and O elements of HTC-1000 (Figure S2). Even when the secondary treatment temperature increases to $1100\text{ }^{\circ}\text{C}$, HTC-1100 still maintains the original bulk morphology,

indicating the high stability of the macrostructure (Figure 2c). TEM and HRTEM images of HTC-1000 have been provided, as shown in Figure S3. It can be seen that a large number of micropores are evenly distributed in the carbon matrix, which is in accordance with the BET analysis. In addition, HTC-1000 shows partially formed graphite nanodomains, indicating that secondary high-temperature carbonization can improve the degree of order (circled in Figure S3b).

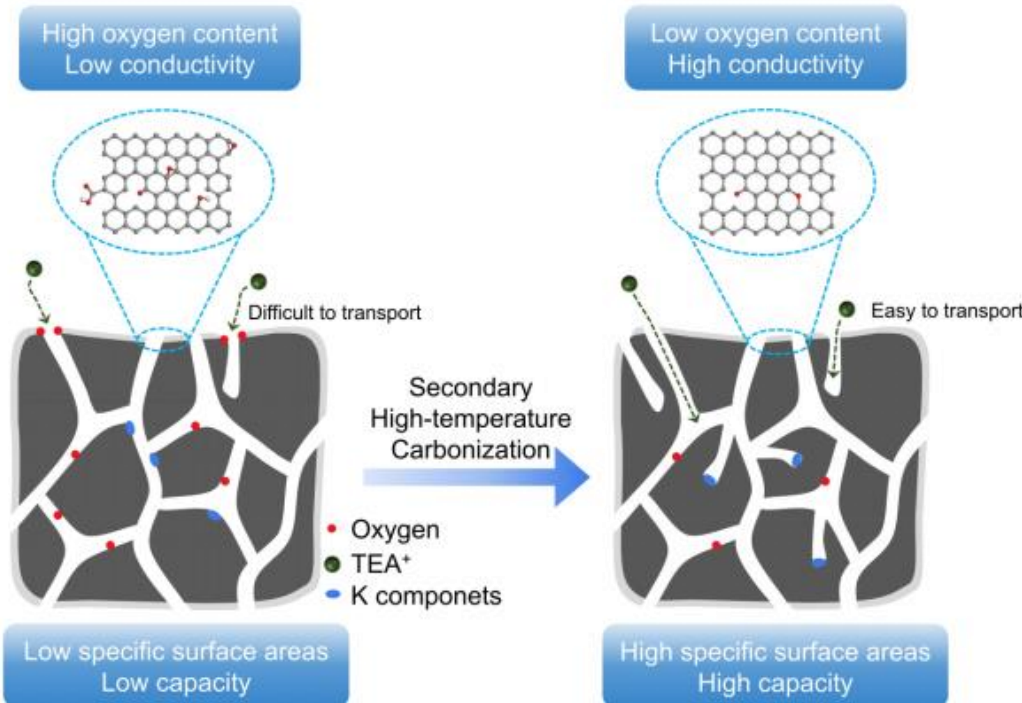


Figure 1. Schematic diagram of preparation process and structure evolution of HTC-1000.

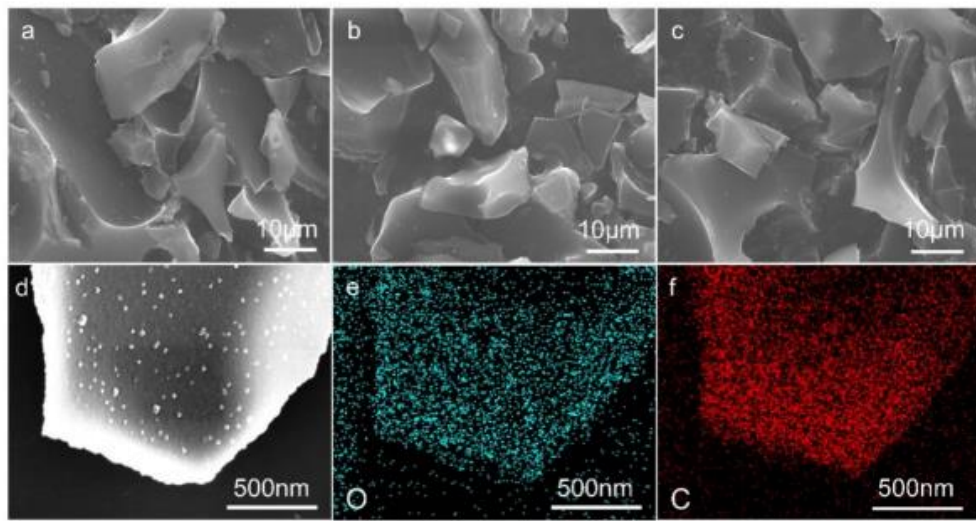


Figure 2. SEM images of (a) HTC-0, (b) HTC-1000, (c) HTC-1100, (d) SEM image of HTC-1000, (e) O mapping of HTC-1000, (f) C mapping of HTC-1000.

To explore the pore structure of the three samples, N_2 adsorption-desorption tests were performed. The vast gas uptake in the low-pressure region is dominated by the micro-porous structures while the adsorption generated in the pressure region of $0.4 < P/P_0 < 0.8$ is dominated by the mesoporous structures. Therefore, from N_2 adsorption–desorption

isotherms, all three samples exhibit pore distribution with both mesoporous and microporous. Moreover, from the hysteresis loop in the N_2 adsorption curve, it is observed that the internal pore type of the material is a slit pore (Figure 3a). According to the Brunauer–Emmett–Teller (BET) method, the untreated HTC-0 shows an SSA of $3156\text{ m}^2\text{ g}^{-1}$, while after second high-temperature treatment, the SSA of HTC-1000 increased to $3333\text{ m}^2\text{ g}^{-1}$. The further increased SSA is due to the secondary activation of residual K components and the release of small gas molecules containing C, H, and O under high temperature [24,25]. The achieved higher SSAs could offer more energy storage active sites for TEA^+ ion adsorption, thus improving capacitance. Moreover, the increased SSAs can increase the effective adsorption area between the capacitor motor and the electrolyte, shorten the diffusion adsorption path of TEA^+ ions in the electrode material, and increase the diffusion speed of particles in the electrode material. However, while the secondary treatment temperature further increased to $1100\text{ }^\circ\text{C}$, the pores in HTC-1100 collapsed, leading to a decreased SSA of $2467\text{ m}^2\text{ g}^{-1}$. Consequently, excessively high temperatures would destroy the pore structure and lead to partial pore blockage, thus adversely affecting the specific capacitance and rate capability of the material. To further investigate the effect of the secondary treatment on the pore structure, the content of micropores and mesopores was analyzed in detail. According to Figure 3b, the total pore volume of HTC-1000 is $2.60\text{ cm}^3\text{ g}^{-1}$, which is much larger than the $2.00\text{ cm}^3\text{ g}^{-1}$ of HTC-0. Furthermore, compared with HTC-0, the micropore volume of HTC-1000 slightly decreased from $1.27\text{ cm}^3\text{ g}^{-1}$ to $1.24\text{ cm}^3\text{ g}^{-1}$ while the mesopore volume has an obvious increase from $0.75\text{ cm}^3\text{ g}^{-1}$ to $1.35\text{ cm}^3\text{ g}^{-1}$, suggesting that high-temperature treatment generates ordered mesoporous pores [26–28]. The expanded pores volume and micropores can effectively promote the transport of the TEA^+ ions and provide plenty of space to store the electrolyte [29,30]. However, the total pore volume of HTC-1100 decreased to $1.69\text{ cm}^3\text{ g}^{-1}$ with the micropore volume decreasing to $0.95\text{ cm}^3\text{ g}^{-1}$ and mesopore volume decreasing to $0.74\text{ cm}^3\text{ g}^{-1}$ due to the pore shrinkage and collapse caused by excessive high-temperature treatment (Table S1). Compared to aqueous systems, organic electrolyte ions are larger (the non-solvated TEA^+ ion sizes are 0.67 nm , respectively), requiring larger pore volumes and higher mesopore ratios to store and transport electrolyte ions [31–34]. The high-temperature treatment at $1000\text{ }^\circ\text{C}$ significantly expands the pore volume and increases the mesopore ratio of the material without significant changes in morphology, providing HTC-1000 with an increased specific capacitance and improved rate performance under high current densities. The pore diameter distribution of the three samples is shown in Figure 3c. The micropore diameter is centered at 1.17 nm , which is beneficial for ion transport, while the mesoporous diameter is centered at $2.7\text{--}4\text{ nm}$, which can form a repository for the electrolyte, quickly providing ions for energy storage during charging and discharging.

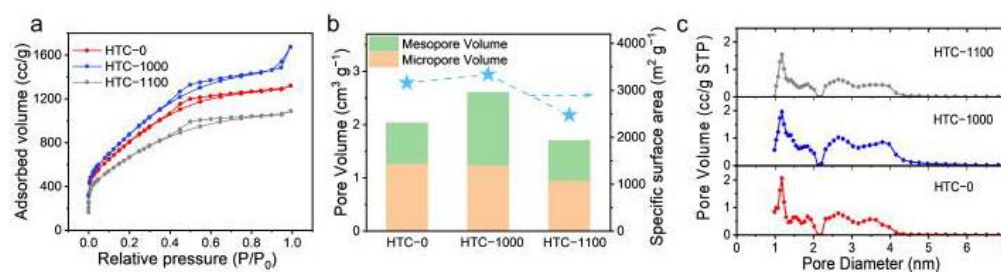


Figure 3. (a) N_2 adsorption-desorption isotherms, (b) porous structure evolution and specific surface area, and (c) pore size distributions of HTCs.

The X-ray diffraction (XRD) patterns of HTCs are shown in Figure 4a. The peaks in the low-angle scattering region of all samples indicate that the material HTCs have a porous structure [35–37]. Due to the non-graphitic disordered stacking and amorphous structure of the porous carbon material, the XRD pattern appears as a bread-like shape and the broad diffraction peaks at around 26° and 43° correspond to the reflections of the (002) and

(100) planes, respectively [38,39]. It can be observed from the pattern that the low-angle scattering intensity of HTC-1000 increases after secondary high-temperature treatment, indicating that HTC-1000 has a more developed porous structure. However, there is no obvious peak shift for HTC-0, HTC-1000, and HTC-1100, illustrating that secondary high-temperature treatment cannot affect the interlayer spacings of graphite nanodomains in these three samples [40]. The intensities of peaks in HTC-1000 and HTC-1100 are stronger than that of HTC-0, indicating an increase in the ordered degree, which contributed to the improvement of conductivity. The Raman spectra of HTCs are shown in Figure 4b. The Raman spectra of three samples showed D and G peaks located at 1350 and 1580 cm⁻¹. The Raman spectra were fitted with four peaks located at 1150, 1350, 1510, and 1580 cm⁻¹, which characterize the T band, D band, D' band, and G band, respectively, where the D band and G band represent sp³-type disordered carbon and sp²-type graphitic carbon, respectively (Figure 4c and Figure S4). The area ratio of the D band and G band (A_D/A_G) can be used to characterize the defect content of the sample. After areas fitting, the A_D/A_G of HTC-0, HTC-1000, and HTC-1100 are 3.28, 2.87, and 2.76, respectively. The decrease in A_D/A_G ratios with an increasing treatment temperature demonstrates the improvement in the crystallinity and graphitization degree, which is identical to the XRD results [41]. As the internal crystal structure of the material becomes more ordered, more conjugated π electrons are formed, and electrons can move freely inside the material, leading to good electrical conductivity [42]. The increase in graphitization during high-temperature treatment produces a more stable crystal structure. This structural stabilization improves the chemical stability of HTC-1000, which results in better cycling stability. The Fourier-transform infrared spectrum of HTC-0 exhibits specific absorption peaks, including 700 cm⁻¹ belonging to -CH in the aromatic ring, 1200 cm⁻¹ caused by C=O, 1500 cm⁻¹ belonging to -CH₃ connected to the aromatic ring, 1600 cm⁻¹ caused by C=C vibration, 2850 cm⁻¹ and 2950 cm⁻¹ belonging to the -CH₂ peak connected to the aromatic ring, and 3700 cm⁻¹ belonging to -OH (Figure 4d, Table S2). After secondary high-temperature treatment, the -OH peak and the C=O peak are significantly weakened in HTC-1000 and HTC-1100, suggesting that the unstable -OH and C=O are further released at high temperatures [43–45]. The removal of oxygen-containing functional groups is beneficial to the properties of porous carbon materials. Firstly, the removal of oxygen-containing functional groups promotes the formation of carbon six-membered rings, which is conducive to the construction of a continuous carbon conductive network and thus improves electrical conductivity. Secondly, since oxygen functional groups are highly reactive, removing them can avoid overmuch side reactions and improve the electrochemical stabilization of the material in SCs. Finally, the removal of oxygen-containing functional groups reduces the impediment for ion transport, creating abundant channels for rapid ion transport. As shown in Figure 4e, the total XPS spectra of HTCs all show O 1s peaks at 532.8 eV and C 1s peaks at 284.8 eV, and the C/O ratio of HTC-0, HTC-1000, and HTC-1100 are 16.1, 19.2, and 21.7, respectively, proving the decreased O content and increased C content after secondary high-temperature carbonization. The enhanced C content illustrates that the secondary high-temperature treatment can effectively remove the unstable oxygen-containing functional groups [46]. As shown in Figure 4f, high-resolution C 1s spectra can be fitted into three peaks centered at 287.9, 285.8, and 284.5 eV, corresponding to C=O, C-O, and C=C bonds, respectively. The ratios of C=C and C-O are 57% and 23% of HTC-0, respectively. After secondary high-temperature treatment, HTC-1000 shows an increased ratio of C=C (60%) and a decreased ratio of C-O (16%). The increase in the C=C bonding ratio indicates the formation of a more complete carbon conducting network in HTC-1000, while the decrease in the C-O bonding ratio suggests that the O impurities are effectively removed.

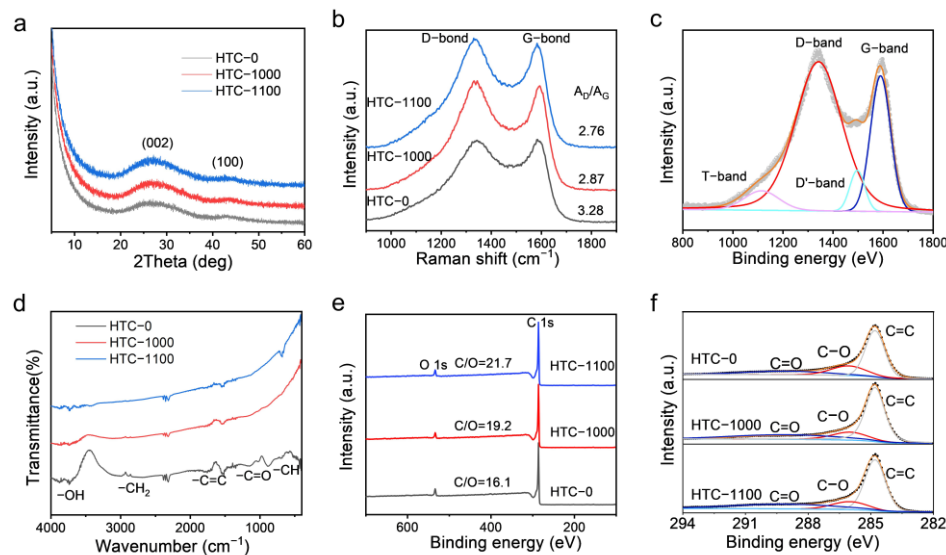


Figure 4. (a) XRD patterns and (b) Raman spectra of HTCs. (c) Raman fit plot of HTC-1000, (d) FTIR spectra, (e) XPS survey spectra, and (f) high-resolution XPS C 1s spectra of the HTCs.

To evaluate the electrochemical performance of HTCs, GCD, CV, rate performance, and cyclic stability, tests were conducted [47]. The active mass loadings of electrodes were 2.0 mg cm^{-2} . CV tests are carried out from 0 to 2.5 V at the scan rate of 10 mV s^{-1} , and the CV curves of HTC-0, HTC-1000, and HTC-1100 are all rectangular-shaped, indicating good double-layer capacitance behavior (Figure 5a). Compared with HTC-0 and HTC-1100, HTC-1000 shows a larger area at the same current, indicating a higher capacitance. The excellent energy storage properties of HTC-1000 benefited from its larger SSAs and more abundant pore distribution, which can provide sufficient active sites. Moreover, the CV tests were carried out at a series of scan rates of 20, 50, 100, and 200 mV s^{-1} . From Figure S5, the shape of CV curves is maintained well, indicating the good stability of HTC-1000. GCD tests were conducted and based on the equation (m is the active mass loading on the single electrode), and HTC-1000 exhibits a high capacitance of 199.2 F g^{-1} at 1 A g^{-1} , which is higher than the 170.4 F g^{-1} of HTC-0 (Figure 5b). When the current densities increase to 2, 3, 4, 5, and 10 A g^{-1} , HTC-1000 exhibits a high capacitance of 189.8, 182.9, 177.9, 173.6, and 158.2 F g^{-1} , respectively. In addition, the GCD curves of HTC-1000 exhibit a standard isosceles triangular shape, meaning that there is no redox reaction in HTC-1000, resulting in the fast charge-discharge capability [48]. As shown in Figure 5c, HTC-0 exhibits a specific capacitance of 170.4 F g^{-1} at 1 A g^{-1} and a specific capacitance of 107.5 F g^{-1} at 20 A g^{-1} , with a capacity retention ratio of 62.9%. After secondary high-temperature treatment, HTC-1000 displays a high specific capacitance of 199.2 F g^{-1} at 1 A g^{-1} . In addition, the capacity retention ratio of HTC-1000 at 20 A g^{-1} increases from 62.9% to 68.3%, with a specific capacitance of 136.3 F g^{-1} (Table S3). The improved capacitance and rate performance benefit from the increased SSAs, abundant mesoporous, and excellent conductivity, which can provide more energy storage sites and promote the transport kinetics of ions and the conduction of electrons [49,50]. In addition, the commonly used YP-50F was also tested for comparing cycling stability. Compared with YP-50F, which displays a specific capacitance of 90.0 F g^{-1} at 1 A g^{-1} and 26.0 F g^{-1} at 20 A g^{-1} , HTC-1000 has a significant advantage (Figure S6). As for HTC-1100, due to the excessively high temperature during secondary high-temperature treatment, some pores collapse and merge, resulting in a decreased specific capacitance of 168.0 F g^{-1} at 1 A g^{-1} and 80.0 F g^{-1} at 20 A g^{-1} . Furthermore, the HTC-1000//HTC-1000 symmetric SCs were also assembled and measured at 1, 5, 10, 20, 30, 40, 50, 70, and 100 A g^{-1} . According to the equation: $E = C(\Delta V)^2 / (8 \times 3.6)$, $P = 3600E / \Delta t$, the HTC-1000//HTC-1000 symmetric SCs exhibit an excellent energy density of 43.2 Wh kg^{-1} at the power density of 625.0 W kg^{-1} , which

is much higher than the other reported carbon material (Figure 5d, Table S5) [48,51–60]. Furthermore, the cycling performance of symmetric organic SCs assembled with HTC-1000 was tested at 5 A g^{-1} . As shown in Figure 5e, even after as long as 50,000 cycles, the symmetric supercapacitor still maintains a high capacitance of 179.0 F g^{-1} , with a high capacity retention ratio of 90%. The outstanding cycling stability of symmetric organic supercapacitors derives from the excellent structural stability of the electrode material and the few side reactions. SEM images of HTC-1000 after cycling for 50,000 cycles still maintain a blocky structure of $20\text{--}40 \mu\text{m}$, which is in accordance with the pristine HTC-1000 (Figure S7). It shows that the electrode material can maintain the structural integrity during charging and discharging, thus improving the cycle stability. Under high pressure in the organic electrolyte, the -COOH groups and C-O groups are easily decomposed to produce H_2O , CO_2 , CO, and other gas molecules, which can raise side reactions and affect electrode stability. Moreover, the oxygen-containing functional groups can react with the electrolyte and catalyze the decomposition of the electrolyte. Therefore, the removal of oxygen-containing functional groups can effectively hinder the occurrence of side reactions and enhance the cycling stability of electrode materials. In general, due to the excellent structural stability of the materials and the decrease in side reactions, symmetric organic supercapacitors assembled with HTC-1000 exhibit outstanding cycling stability.

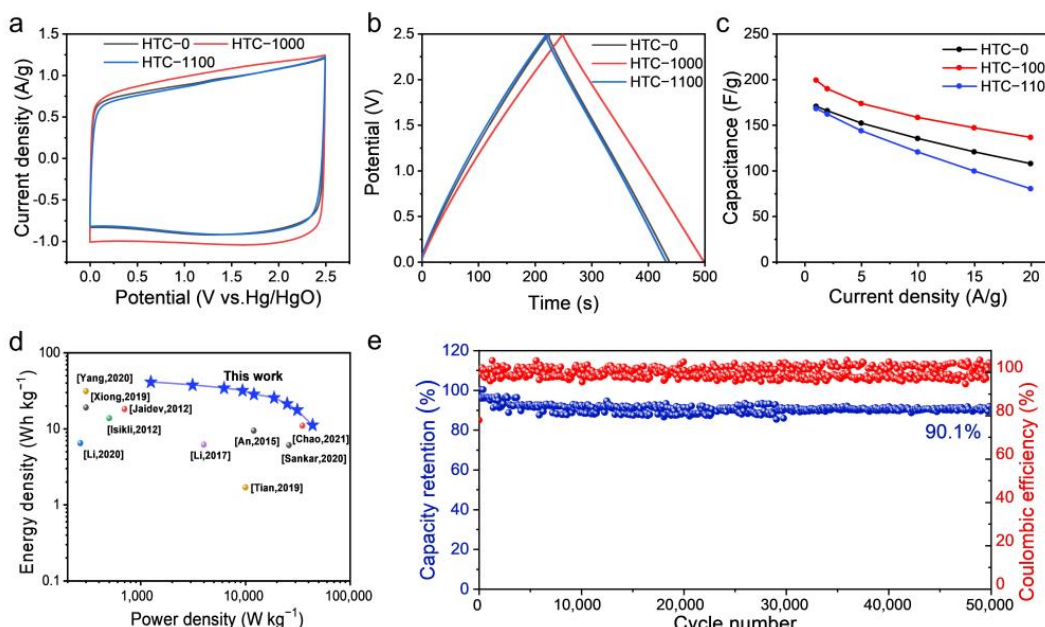


Figure 5. (a) CV curves at 10 mV s^{-1} , (b) galvanostatic charge–discharge curves at 1 A g^{-1} , (c) gravimetric capacitance, (d) Ragone plots [48,51–60], (e) Cycle performance with the mass loading of 2 mg cm^{-2} at 5 A g^{-1} .

Electrochemical impedance tests were conducted to explore the ionic and electronic conductivity. According to the Nyquist plots of HTCs, HTC-1000 treated at high temperature exhibits better electronic transport efficiency and conductivity compared with HTC-0 (Figure 6a) [61,62]. To further analyze the effects of secondary high-temperature treatment on ionic conductivity and electronic conductivity, the Nyquist plots have been fitted and the corresponding equivalent electrical circuit diagram is shown in Figure S8. The electrode resistances obtained from equivalent circuits by fitting the experimental data of HTCs electrodes are shown in Table S4. According to the fitted data, the R_{ct} of HTC-1000 and HTC-1100 are 5.7Ω and 2.5Ω , which are much lower than that of HTC-0 16.2 . It shows that secondary high-temperature treatment can effectively improve electronic conductivity. As shown in Figure S9, the slope between Z' and $\omega^{-1/2}$ represents the Warburg coefficient (σ_w). The slopes of HTC-0, HTC-1000, and HTC-1100 are 2.9, 2.7, and 4.1, respectively,

indicating the highest diffusion coefficient of HTC-1000. This is because after secondary high-temperature treatment, the porosity of HTC-1000 is expanded and more mesoporous is formed. However, the high temperature of HTC-1100 leads to the collapse of pore structures, resulting in lower ion transport efficiency. To further verify the conductivity of the samples, we measured the I-V curves of the sample HTCs with an electrochemical workstation. From Figure 6b,c, it can be found that the conductivities of HTC-0, HTC-1000, and HTC-1100 are 58.4, 68.6, and 97.4 S m^{-1} , respectively, which is consistent with the R_{ct} results.

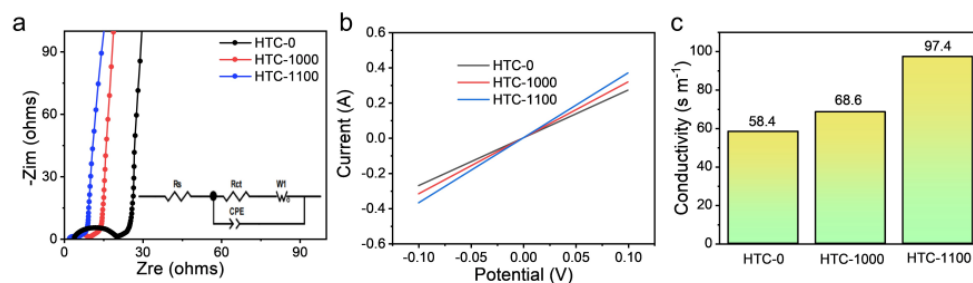


Figure 6. (a) Nyquist plots, (b) I-V curves, (c) conductivity of HTCs.

4. Conclusions

In conclusion, we have fabricated a kind of porous carbon with both high SSAs and excellent conductivity via the secondary high-temperature treatment strategy. Firstly, the enhanced SSAs and micropores of the porous carbon material provide more reactive active sites, leading to increased specific capacitance. Moreover, the more complete carbon six-numbered rings due to oxygen elimination effectively improve the conductivity of the material, which results in better rate performance. In addition, rapid ion transport has been achieved and benefited from the elimination of oxygen. As a result, the synthesized anode displays a high specific capacitance of 199.2 F g^{-1} at 1 A g^{-1} , and the assembled symmetrical supercapacitor has an outstanding energy density of 43.2 Wh kg^{-1} at a power density of 625.0 W kg^{-1} . The strategy can provide novel enlightenment for designing porous carbon in the energy storage field.

Supplementary Materials: The following supporting information can be downloaded at: <https://www.mdpi.com/article/10.3390/batteries10010005/s1>; Figure S1: SEM images of (a,b) HTC-0, (c,d) HTC-1000, (e,f) HTC-1100; Figure S2: The EDS spectrum of HTC-1000; Figure S3. (a) TEM images of HTC-1000 and (b) HRTEM images of HTC-1000; Figure S4: Raman spectra of (a) HTC-0, (b) HTC-1100; Figure S5: CV curves at different scan rates and galvanostatic charge-discharge curves at different current densities of the (a,b) HTC-0, (c,d) HTC-1000, (e,f) HTC-1100; Figure S6: Gravimetric capacitance of YP-50F; Figure S7: SEM images of after cycling HTC-1000; Figure S8: (a) Nyquist plots and (b) the corresponding equivalent electrical circuit; Figure S9: line plots between Z' and $\omega^{-1/2}$. Table S1: Texture properties of HTCs measured by N_2 adsorption-desorption isotherms; Table S2. Peaks attribution in FTIR spectra of porous carbons; Table S3: Specific capacitance of HTC-0, HTC-1000, HTC-1100, and YP-50F; Table S4: Fitting experimental resistances of HTCs electrodes; Table S5: Electrochemical performance comparison between the HTC-1000//HTC-1000 symmetric device and other devices.

Author Contributions: Conceptualization, Z.F.; methodology, validation, writing—original draft preparation, W.C.; formal analysis, writing—review and editing, C.C.; writing—review and editing, G.W.; writing—review and editing, Z.Q.; software, Q.L.; resources, T.W.; Visualization, Z.X.; Visualization, Z.L.; Visualization, B.Q.; Visualization, K.C. All authors have read and agreed to the published version of the manuscript.

Funding: This research was funded by the National Natural Science Foundation of China, grant number 52202311, 51972342, 51872056, Shandong Provincial Natural Science Foundation, China, grant number ZR2020QE050, Fundamental Research Funds for the Central Universities, grant number

20CX06024A, Key Basic Research Projects of Natural Science Foundation of Shandong province, grant number ZR2019ZD51, Taishan Scholar Project of Shandong Province, grant number ts20190922.

Data Availability Statement: All created data are contained in the manuscript and the Supporting Information.

Conflicts of Interest: The authors declare no conflicts of interest.

References

- Zhu, Y.W.; Murali, S.; Stoller, M.D.; Ganesh, K.J.; Cai, W.W.; Ferreira, P.J.; Pirkle, A.; Wallace, R.M.; Cychoz, K.A.; Thommes, M.; et al. Carbon-based supercapacitors produced by activation of graphene. *Science* **2011**, *332*, 1537–1541. [CrossRef] [PubMed]
- Yu, Z.N.; Tetard, L.; Zhai, L.; Thomas, J. Supercapacitor electrode materials: Nanostructures from 0 to 3 dimensions. *Energy Environ. Sci.* **2015**, *8*, 702–730. [CrossRef]
- Gogotsi, Y.; Nikitin, A.; Ye, H.H.; Zhou, W.; Fischer, J.E.; Yi, B.; Foley, H.C.; Barsoum, M.W. Nanoporous carbide-derived carbon with tunable pore size. *Nat. Mater.* **2003**, *2*, 591–594. [CrossRef] [PubMed]
- Fan, Z.J.; Liu, Y.; Yan, J.; Ning, G.Q.; Wang, Q.; Wei, T.; Zhi, L.J.; Wei, F. Template-directed synthesis of pillared-porous carbon nanosheet architectures: High-performance electrode materials for supercapacitors. *Adv. Energy Mater.* **2012**, *2*, 419–424. [CrossRef]
- Pang, Z.Y.; Li, G.S.; Xiong, X.L.; Ji, L.; Xu, Q.; Zou, X.L.; Lu, X.G. Molten salt synthesis of porous carbon and its application in supercapacitors: A review. *J. Energy Chem.* **2021**, *61*, 622–640. [CrossRef]
- Tian, W.H.; Zhu, J.Y.; Dong, Y.; Zhao, J.; Li, J.; Guo, N.N.; Lin, H.; Zhang, S.; Jia, D.Z. Micelle-induced assembly of graphene quantum dots into conductive porous carbon for high rate supercapacitor electrodes at high mass loadings. *Carbon* **2020**, *161*, 89–96. [CrossRef]
- Zhang, S.; Zhu, J.Y.; Qing, Y.; Wang, L.X.; Zhao, J.; Li, J.; Tian, W.H.; Jia, D.Z.; Fan, Z.J. Ultramicroporous carbons puzzled by graphene quantum dots: Integrated high gravimetric, volumetric, and areal capacitances for supercapacitors. *Adv. Funct. Mater.* **2018**, *28*, 10. [CrossRef]
- Li, P.; Li, H.; Han, D.L.; Shang, T.X.; Deng, Y.Q.; Tao, Y.; Lv, W.; Yang, Q.H. Packing activated carbons into dense graphene network by capillarity for high volumetric performance supercapacitors. *Adv. Sci.* **2019**, *6*, 8. [CrossRef]
- Li, Q.Q.; Jiang, Y.T.; Jiang, Z.M.; Zhu, J.Y.; Gan, X.M.; Qin, F.W.; Tang, T.T.; Luo, W.X.; Guo, N.N.; Liu, Z.; et al. Ultrafast pore-tailoring of dense microporous carbon for high volumetric performance supercapacitors in organic electrolyte. *Carbon* **2022**, *191*, 19–27. [CrossRef]
- Wang, Q.; Yan, J.; Fan, Z.J. Carbon materials for high volumetric performance supercapacitors: Design, progress, challenges and opportunities. *Energy Environ. Sci.* **2016**, *9*, 729–762. [CrossRef]
- Chang, P.P.; Wang, C.Y.; Kinumoto, T.; Tsumura, T.; Chen, M.M.; Toyoda, M. Frame-filling C/C composite for high-performance EDLCs with high withstand voltage. *Carbon* **2018**, *131*, 184–192. [CrossRef]
- Leng, C.Y.; Zhao, Z.B.; Song, Y.Z.; Sun, L.L.; Fan, Z.J.; Yang, Y.Z.; Liu, X.G.; Wang, X.Z.; Qiu, J.S. 3D carbon frameworks for ultrafast charge/discharge rate supercapacitors with high energy-power density. *Nano-Micro Lett.* **2021**, *13*, 11. [CrossRef] [PubMed]
- Zhu, X.Q.; Yu, S.; Xu, K.T.; Zhang, Y.; Zhang, L.M.; Lou, G.B.; Wu, Y.T.; Zhu, E.H.; Chen, H.; Shen, Z.H.; et al. Sustainable activated carbons from dead ginkgo leaves for supercapacitor electrode active materials. *Chem. Eng. Sci.* **2018**, *181*, 36–45. [CrossRef]
- Gomibuchi, E.; Ichikawa, T.; Kimura, K.; Isobe, S.; Nabeta, K.; Fujii, H. Electrode properties of a double layer capacitor of nano-structured graphite produced by ball milling under a hydrogen atmosphere. *Carbon* **2006**, *44*, 983–988. [CrossRef]
- Zhong, C.; Deng, Y.D.; Hu, W.B.; Qiao, J.L.; Zhang, L.; Zhang, J.J. A review of electrolyte materials and compositions for electrochemical supercapacitors. *Chem. Soc. Rev.* **2015**, *44*, 7484–7539. [CrossRef] [PubMed]
- Peng, H.R.; Yao, B.; Wei, X.J.; Liu, T.Y.; Kou, T.Y.; Xiao, P.; Zhang, Y.H.; Li, Y. Pore and heteroatom engineered carbon foams for supercapacitors. *Adv. Energy Mater.* **2019**, *9*, 9. [CrossRef]
- Jiang, Y.T.; Li, J.; Jiang, Z.M.; Shi, M.J.; Sheng, R.; Liu, Z.; Zhang, S.; Cao, Y.L.; Wei, T.; Fan, Z.J. Large-surface-area activated carbon with high density by electrostatic densification for supercapacitor electrodes. *Carbon* **2021**, *175*, 281–288. [CrossRef]
- Pérez, C.R.; Yeon, S.H.; Ségalini, J.; Presser, V.; Taberna, P.L.; Simon, P.; Gogotsi, Y. Structure and electrochemical performance of carbide-derived carbon nanopowders. *Adv. Funct. Mater.* **2013**, *23*, 1081–1089. [CrossRef]
- Wu, L.Q.; Li, W.W.; Li, P.; Liao, S.T.; Qiu, S.Q.; Chen, M.L.; Guo, Y.F.; Li, Q.; Zhu, C.; Liu, L.W. Powder, paper and foam of few-layer graphene prepared in high yield by electrochemical intercalation exfoliation of expanded graphite. *Small* **2014**, *10*, 1421–1429. [CrossRef]
- Zheng, Q.W.; Li, X.M.; Yang, Q.Z.; Li, C.M.; Liu, G.Q.; Wang, Y.C.; Sun, P.C.; Tian, H.M.; Wang, C.H.; Chen, X.L.; et al. High performance solid-state supercapacitors based on highly conductive organogel electrolyte at low temperature. *J. Power Sources* **2022**, *524*, 10. [CrossRef]
- Wang, Q.; Liu, F.Y.; Jin, Z.Y.; Qiao, X.R.; Huang, H.C.; Chu, X.; Xiong, D.; Zhang, H.T.; Liu, Y.; Yang, W.Q. Hierarchically divacancy defect building dual-activated porous carbon fibers for high-performance energy-storage devices. *Adv. Funct. Mater.* **2020**, *30*, 8. [CrossRef]

22. Vonlanthen, D.; Lazarev, P.; See, K.A.; Wudl, F.; Heeger, A.J. A stable polyaniline-benzoquinone-hydroquinone supercapacitor. *Adv. Mater.* **2014**, *26*, 5095–5100. [[CrossRef](#)]
23. Heon, M.; Lofland, S.; Applegate, J.; Nolte, R.; Cortes, E.; Hettinger, J.D.; Taberna, P.L.; Simon, P.; Huang, P.H.; Brunet, M.; et al. Continuous carbide-derived carbon films with high volumetric capacitance. *Energy Environ. Sci.* **2011**, *4*, 135–138. [[CrossRef](#)]
24. Wu, J.Y.; Zhang, X.; Ju, Z.Y.; Wang, L.; Hui, Z.Y.; Mayilvahanan, K.; Takeuchi, K.J.; Marschilok, A.C.; West, A.C.; Takeuchi, E.S.; et al. From fundamental understanding to engineering design of high-performance thick electrodes for scalable energy-storage systems. *Adv. Mater.* **2021**, *33*, 16. [[CrossRef](#)]
25. Liu, H.Y.; Xu, T.; Cai, C.Y.; Liu, K.; Liu, W.; Zhang, M.; Du, H.S.; Si, C.L.; Zhang, K. Multifunctional superelastic, superhydrophilic, and ultralight nanocellulose-based composite carbon aerogels for compressive supercapacitor and strain sensor. *Adv. Funct. Mater.* **2022**, *32*, 12. [[CrossRef](#)]
26. Zornitta, R.L.; Barcelos, K.M.; Nogueira, F.G.E.; Ruotolo, L.A.M. Understanding the mechanism of carbonization and KOH activation of polyaniline leading to enhanced electrosorption performance. *Carbon* **2020**, *156*, 346–358. [[CrossRef](#)]
27. Chmiola, J.; Yushin, G.; Gogotsi, Y.; Portet, C.; Simon, P.; Taberna, P.L. Anomalous increase in carbon capacitance at pore sizes less than 1 nanometer. *Science* **2006**, *313*, 1760–1763. [[CrossRef](#)]
28. Huang, C.; Tang, Q.L.; Feng, Q.S.; Li, Y.H.; Xu, Y.L.; Zhang, Y.; Hu, A.; Zhang, S.Y.; Deng, W.N.; Chen, X.H. Achieving ultrahigh volumetric performance of graphene composite films by an outer-inner dual space utilizing strategy. *J. Mater. Chem. A* **2020**, *8*, 9661–9669. [[CrossRef](#)]
29. Shao, H.; Wu, Y.C.; Lin, Z.F.; Taberna, P.L.; Simon, P. Nanoporous carbon for electrochemical capacitive energy storage. *Chem. Soc. Rev.* **2020**, *49*, 3005–3039. [[CrossRef](#)]
30. Wang, Y.G.; Song, Y.F.; Xia, Y.Y. Electrochemical capacitors: Mechanism, materials, systems, characterization and applications. *Chem. Soc. Rev.* **2016**, *45*, 5925–5950. [[CrossRef](#)]
31. Pan, B.Y.G.; Bai, L.; Hu, C.M.; Wang, X.P.; Li, W.S.; Zhao, F.G. Graphene-indanthrone donor- π -acceptor heterojunctions for high-performance flexible supercapacitors. *Adv. Energy Mater.* **2020**, *10*, 8. [[CrossRef](#)]
32. Sevilla, M.; Ferrero, G.A.; Diez, N.; Fuertes, A.B. One-step synthesis of ultra-high surface area nanoporous carbons and their application for electrochemical energy storage. *Carbon* **2018**, *131*, 193–200. [[CrossRef](#)]
33. Salanne, M.; Rotenberg, B.; Naoi, K.; Kaneko, K.; Taberna, P.L.; Grey, C.P.; Dunn, B.; Simon, P. Efficient storage mechanisms for building better supercapacitors. *Nat. Energy* **2016**, *1*, 10. [[CrossRef](#)]
34. Xu, L.; Shi, R.Y.; Li, H.F.; Han, C.P.; Wu, M.Y.; Wong, C.P.; Kang, F.Y.; Li, B.H. Pseudocapacitive anthraquinone modified with reduced graphene oxide for flexible symmetric all-solid-state supercapacitors. *Carbon* **2018**, *127*, 459–468. [[CrossRef](#)]
35. Yang, X.W.; Cheng, C.; Wang, Y.F.; Qiu, L.; Li, D. Liquid-mediated dense integration of graphene materials for compact capacitive energy storage. *Science* **2013**, *341*, 534–537. [[CrossRef](#)]
36. Wang, C.J.; Liu, F.; Chen, J.S.; Yuan, Z.W.; Liu, C.; Zhang, X.S.; Xu, M.Y.; Wei, L.; Chen, Y. A graphene-covalent organic framework hybrid for high-performance supercapacitors. *Energy Storage Mater.* **2020**, *32*, 448–457. [[CrossRef](#)]
37. Yang, B.J.; Chen, J.T.; Lei, S.L.; Guo, R.S.; Li, H.X.; Shi, S.Q.; Yan, X.B. Spontaneous growth of 3D framework carbon from sodium citrate for high energy- and power-density and long-life sodium-ion hybrid capacitors. *Adv. Energy Mater.* **2018**, *8*, 11. [[CrossRef](#)]
38. Peng, L.; Hung, C.T.; Wang, S.W.; Zhang, X.M.; Zhu, X.H.; Zhao, Z.W.; Wang, C.Y.; Tang, Y.; Li, W.; Zhao, D.Y. Versatile nanoemulsion assembly approach to synthesize functional mesoporous carbon nanospheres with tunable pore sizes and architectures. *J. Am. Chem. Soc.* **2019**, *141*, 7073–7080. [[CrossRef](#)]
39. Sutarsis; Patra, J.; Su, C.Y.; Li, J.; Bresser, D.; Passerini, S.; Chang, J.K. Manipulation of nitrogen-heteroatom configuration for enhanced charge-storage performance and reliability of nanoporous carbon electrodes. *ACS Appl. Mater. Interfaces* **2020**, *12*, 32797–32805. [[CrossRef](#)]
40. Liang, Y.R.; Liang, F.X.; Zhong, H.; Li, Z.H.; Fu, R.W.; Wu, D.C. An advanced carbonaceous porous network for high-performance organic electrolyte supercapacitors. *J. Mater. Chem. A* **2013**, *1*, 7000–7005. [[CrossRef](#)]
41. Yang, I.; Yoo, J.; Kwon, D.; Choi, D.; Kim, M.S.; Jung, J.C. Improvement of a commercial activated carbon for organic electric double-layer capacitors using a consecutive doping method. *Carbon* **2020**, *160*, 45–53. [[CrossRef](#)]
42. Wu, X.; Liu, R.; Zhao, J.; Fan, Z. Advanced carbon materials with different spatial dimensions for supercapacitors. *Nano Mater. Sci.* **2021**, *3*, 241–247. [[CrossRef](#)]
43. Fan, Z.J.; Wang, K.; Wei, T.; Yan, J.; Song, L.P.; Shao, B. An environmentally friendly and efficient route for the reduction of graphene oxide by aluminum powder. *Carbon* **2010**, *48*, 1686–1689. [[CrossRef](#)]
44. Hsu, H.L.; Miah, M.; Saha, S.K.; Chen, J.H.; Chen, L.C.; Hsu, S.Y. Three-dimensional bundle-like multiwalled carbon nanotubes composite for supercapacitor electrode application. *Mater. Today Chem.* **2021**, *22*, 10. [[CrossRef](#)]
45. Guo, W.; Yu, C.; Li, S.F.; Qiu, J.S. Toward commercial-level mass-loading electrodes for supercapacitors: Opportunities, challenges and perspectives. *Energy Environ. Sci.* **2021**, *14*, 576–601. [[CrossRef](#)]
46. Guo, J.B.; Li, L.; Luo, J.; Gong, W.N.; Pan, R.; He, B.; Xu, S.H.; Liu, M.N.; Wang, Y.J.; Zhang, B.H.; et al. Polypyrrole-assisted nitrogen doping strategy to boost vanadium dioxide performance for wearable nonpolarity supercapacitor and aqueous Zinc-Ion battery. *Adv. Energy Mater.* **2022**, *12*, 12. [[CrossRef](#)]
47. Raj, C.J.; Manikandan, R.; Thondaiman, P.; Sivakumar, P.; Savariraj, A.D.; Cho, W.J.; Kim, B.C.; Jung, H. Sonoelectrochemical exfoliation of graphene in various electrolytic environments and their structural and electrochemical properties. *Carbon* **2021**, *184*, 266–276. [[CrossRef](#)]

48. Li, F.F.; Wang, X.L.; Sun, R.C. A metal-free and flexible supercapacitor based on redox-active lignosulfonate functionalized graphene hydrogels. *J. Mater. Chem. A* **2017**, *5*, 20643–20650. [[CrossRef](#)]
49. Long, S.S.; Feng, Y.C.; He, F.L.; Zhao, J.Z.; Bai, T.; Lin, H.B.; Cai, W.L.; Mao, C.W.; Chen, Y.H.; Gan, L.H.; et al. Biomass-derived, multifunctional and wave-layered carbon aerogels toward wearable pressure sensors, supercapacitors and triboelectric nanogenerators. *Nano Energy* **2021**, *85*, 11. [[CrossRef](#)]
50. Xie, K.; Qin, X.T.; Wang, X.Z.; Wang, Y.N.; Tao, H.S.; Wu, Q.; Yang, L.J.; Hu, Z. Carbon nanocages as supercapacitor electrode materials. *Adv. Mater.* **2012**, *24*, 347–352. [[CrossRef](#)]
51. Yang, Y.Y.; Ma, W.X.; Zhu, H.; Meng, H.X.; Wang, C.J.; Ma, F.Q.; Hu, Z.A. Graphene covalently functionalized with 2,6-diaminoanthraquinone (DQ) as a high performance electrode material for supercapacitors. *New J. Chem.* **2020**, *44*, 16821–16830. [[CrossRef](#)]
52. Tian, M.; Wu, J.W.; Li, R.H.; Chen, Y.L.; Long, D.H. Fabricating a high-energy-density supercapacitor with asymmetric aqueous redox additive electrolytes and free-standing activated-carbon-felt electrodes. *Chem. Eng. J.* **2019**, *363*, 183–191. [[CrossRef](#)]
53. Isikli, S.; Díaz, R. Substrate-dependent performance of supercapacitors based on an organic redox couple impregnated on carbon. *J. Power Sources* **2012**, *206*, 53–58. [[CrossRef](#)]
54. Xiong, C.L.; Zou, Y.B.; Peng, Z.Y.; Zhong, W.B. Synthesis of morphology-tunable electroactive biomass/graphene composites using metal ions for supercapacitors. *Nanoscale* **2019**, *11*, 7304–7316. [[CrossRef](#)]
55. An, N.; An, Y.F.; Hu, Z.G.; Guo, B.S.; Yang, Y.Y.; Lei, Z.Q. Graphene hydrogels non-covalently functionalized with alizarin: An ideal electrode material for symmetric supercapacitors. *J. Mater. Chem. A* **2015**, *3*, 22239–22246. [[CrossRef](#)]
56. Jaidev; Ramaprabhu, S. Poly(p-phenylenediamine)/graphene nanocomposites for supercapacitor applications. *J. Mater. Chem.* **2012**, *22*, 18775–18783. [[CrossRef](#)]
57. Tian, W.Q.; Gao, Q.M.; Tan, Y.L.; Yang, K.; Zhu, L.H.; Yang, C.X.; Zhang, H. Bio-inspired beehive-like hierarchical nanoporous carbon derived from bamboo-based industrial by-product as a high performance supercapacitor electrode material. *J. Mater. Chem. A* **2015**, *3*, 5656–5664. [[CrossRef](#)]
58. Chao, Y.Z.; Chen, S.B.; Xiao, Y.C.; Hu, X.J.; Lu, Y.; Chen, H.Q.; Xin, S.X.; Bai, Y.X. Ordinary filter paper-derived hierarchical pore structure carbon materials for supercapacitor. *J. Energy Storage* **2021**, *35*, 7. [[CrossRef](#)]
59. Sankari, M.S.; Vivekanandhan, S. Jatropha oil cake based activated carbon for symmetric supercapacitor application: A comparative study on conventional and hydrothermal carbonization processes. *ChemistrySelect* **2020**, *5*, 1375–1384. [[CrossRef](#)]
60. Li, H.; Zhang, X.F.; Wang, X.T.; Zhang, J.Y.; Yang, Y.K. One-pot solvothermal incorporation of graphene into chain-engineered polyquinones for metal-free supercapacitors. *Chem. Commun.* **2020**, *56*, 11191–11194. [[CrossRef](#)]
61. Xue, Q.; Gan, H.B.; Huang, Y.; Zhu, M.S.; Pei, Z.X.; Li, H.F.; Deng, S.Z.; Liu, F.; Zhi, C.Y. Boron element nanowires electrode for supercapacitors. *Adv. Energy Mater.* **2018**, *8*, 8. [[CrossRef](#)]
62. Xu, Y.X.; Lin, Z.Y.; Zhong, X.; Huang, X.Q.; Weiss, N.O.; Huang, Y.; Duan, X.F. Holey graphene frameworks for highly efficient capacitive energy storage. *Nat. Commun.* **2014**, *5*, 8. [[CrossRef](#)] [[PubMed](#)]

Disclaimer/Publisher’s Note: The statements, opinions and data contained in all publications are solely those of the individual author(s) and contributor(s) and not of MDPI and/or the editor(s). MDPI and/or the editor(s) disclaim responsibility for any injury to people or property resulting from any ideas, methods, instructions or products referred to in the content.